Article

Understanding the effect of microstructure and composition on localized corrosion susceptibility of 6xxx aluminum alloys

Check for updates

Priyanka Adapala [1], Thomas Avey[1], Yudie Yuan[2], Mary Lyn Lim[2], Ganesh Bhaskaran [2], Sazol Das[2], Alan Luo [1] & Gerald S. Frankel [1] ✉

The corrosion performance of 6xxx series Al alloys has been found to depend on small changes in composition and microstructure. The corrosion behaviors of three aluminum alloys, AA6111, AA6451, and AA6016, were investigated. AA6111, containing primarily α (Al_{15} $(Fe,Mn)_3Si_2$) intermetallic particles (IMPs), and AA6016, containing primarily β (Al_8Fe_2Si) IMPs, exhibited the best and the worst overall corrosion performances, respectively, as indicated by the extent of corrosion in exposure tests. However, this ranking was not predicted by the standard interpretation of potentiodynamic polarization curves measured on the alloys. The corrosion susceptibilities of the three alloys were further investigated by evaluating the electrochemical behavior of the component phases separately. Bulk analogs of the component phases were fabricated using standard alloy casting techniques. The fabricated bulk analogs of α and β IMPs, as well as the three alloy matrix phases, were tested using either macrocell or microcell testing. An explanation for the alloy performances was developed by combining the behavior of the component phases.

Pure Al is generally considered corrosion resistant due to the protective nature of spontaneously forming aluminum oxide passive film[1–4]. The passive film is a wide bandgap insulator that does not strongly support electrochemical reactions. Even if the passive film on pure Al is slightly scratched or breaks down locally, the rest of the surface oxide can only provide a limited cathodic current to support the local anodic attack. To improve the mechanical properties of Al alloys, particular microstructures are developed by appropriate alloying additions and heat treatments[1,4,5]. However, most Al alloys are susceptible to localized corrosion because the intermetallic particles (IMPs) resulting from alloying and subsequent heat treatment act as either active sites for film breakdown or efficient cathodes to support any anodic attack. In most cases, the continuous matrix and the IMPs in Al alloys exhibit different electrochemical behavior, which can cause localized corrosion[6]. The localized corrosion initiation is often associated with IMPs acting as local cathodes supporting the oxygen reduction reaction (ORR) and driving dissolution or pitting attack at the particle-matrix interface or nearby region[1,4,6,7].

6xxx series aluminum alloys (AA6xxx) are heat-treatable alloys containing Mg and Si as the two principal alloying elements. Their primary strengthening mechanism is age hardening, resulting in the precipitation of Mg_2Si[8]. AA6xxx are known for their excellent specific strength, formability, and plasticity, and as a result, have found applications in the infrastructure, automobile, and machinery industries[8–10]. The automotive industry is targeting fuel conservation by vehicle weight reduction through the incorporation of lighter materials such as aluminum alloys[11]. In general, AA6xxx exhibits good corrosion resistance. However, in applications where AA6xxx are exposed to aggressive environments such as road deicing salts, marine atmospheres, mud, and other environmental pollutants, they are susceptible to localized corrosion[12].

The alloying element Cu can have diverse effects on the corrosion susceptibility of AA6xxx. The literature contains reports with contradictory evidence of the effect of Cu when present in IMPs and in solid solutions. Muller et al.[13] reported an increase in the pitting potentials of Al-Cu binary alloys as a result of increase in Cu content in the matrix solid solution. In general, the presence of noble elements such as Cu in a solid solution makes

[1]The Ohio State University, 4136 Fontana Laboratories, 140 W 19th Ave Building 151, Columbus, OH 43210, USA. [2]Novelis Global R&T Center, Kennesaw, GA 30144, USA. ✉e-mail: frankel.10@osu.edu

1

Table 1 | Elemental composition ranges of AA6xxx alloys studied

Alloys/Element wt.%	Si	Fe	Cu	Mn	Mg	Ti	Zn	Cr	Excess Si	Al
AA6111	0.60–1.1	≤0.4	0.5–0.9	0.1–0.45	0.5–1	≤0.1	≤0.15	≤0.10	0.12	Balance
AA6451	0.60–1	≤0.4	≤0.4	0.05–0.4	0.4–0.8	≤0.1	≤0.15	≤0.10	0.27	
AA6016	1–1.5	≤0.4	≤0.2	≤0.2	0.25-0.6	≤0.15	≤0.20	≤0.10	1.17	

*From www.matweb.com.

Fig. 1 | Optical micrographs of AA6xxx-T4 + PB, top surfaces, as-polished condition. AA6111 (top left), AA6451 (top right) and AA6016 (bottom).
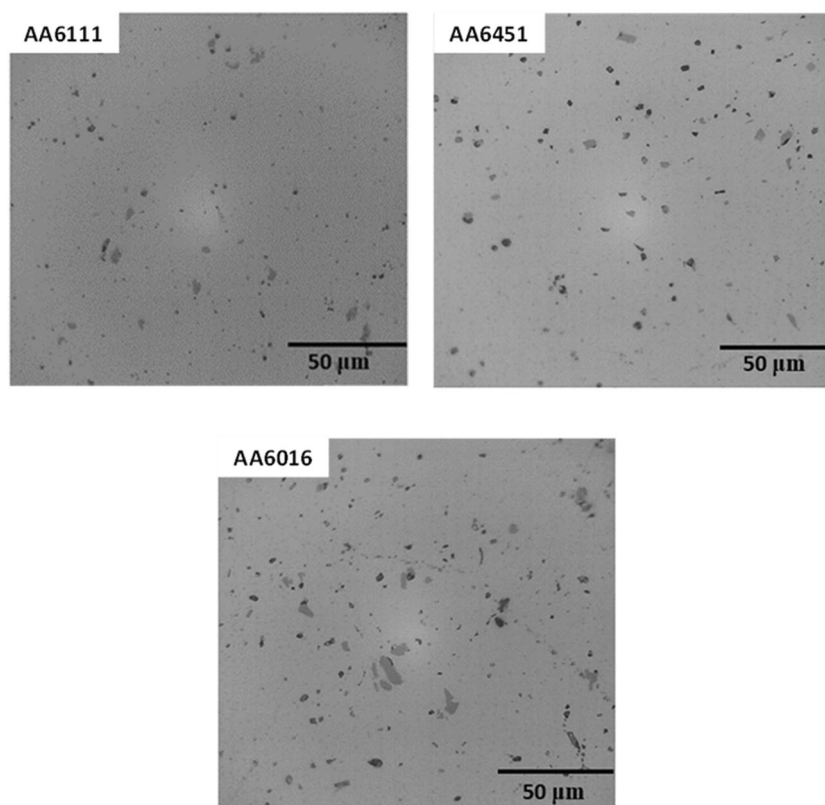
the matrix more noble and less susceptible to corrosion, resulting in a decreased susceptibility to localized corrosion. Several authors have described the effects of aging treatment and composition on intergranular corrosion susceptibility (IGC) of AA6xxx alloys, mostly in acidic chloride solutions. Larsen et al. reported how, in the underaged condition, segregation of a continuous Cu-rich nanofilm along the grain boundaries led to a solute-depleted zone adjacent to the grain boundary, resulting in microgalvanic coupling and preferential attack[14,15]. However, upon peak aging, the continuous Cu-rich film was disrupted due to discrete Q-phase ($Al_4Cu_2Mg_8Si_7$) precipitation, resulting in reduced IGC susceptibility. Zou et al.[16] also found that AA6xxx alloys could be susceptible to IGC depending on the Cu content, the Mg/Si ratio, and the continuity of the IMPs on the grain boundaries. Svenningsen et al.[17,18] studied the effect of artificial aging on IGC susceptibility of AA6xxx with low Cu content and found that artificial aging is more beneficial than natural aging in improving the resistance to IGC. Kairy and coworkers systematically varied the Cu content and Si/Mg ratio, finding that increasing the Cu content and Si/Mg ratio increased IGC severity[19,20]. Thermal treatment also impacted the extent of the attack by influencing the grain boundary microstructure.

Fe, the most common impurity present in commercial aluminum alloys, is extremely detrimental to corrosion resistance as it exhibits very low solid solubility in the Al-matrix (~0.052 wt.% at 655 °C) and tends to form irregularly shaped coarse IMPs with dimensions ranging from tens to a few tenths of a micrometer[21–24]. Park et al.[25] studied the influence of Al_3Fe

inclusions on pitting corrosion of AA6061 in chloride environments. Al_3Fe intermetallic inclusions served as local cathodes supporting ORR. The pH around the IMPs increased, resulting in dissolution of the matrix and the formation of cavities in the host metal. Birbilis et al.[24] evaluated the effect of Al_7Cu_2Fe on the electrochemical behavior and localized corrosion of AA7075. Al_7Cu_2Fe IMPs are cathodic to the alloy matrix and can sustain ORR at appreciable rates of ~20 µA cm−2 to 2 mA cm^{-2} depending on pH and chloride concentration. The ORR rate on Al_7Cu_2Fe increases with increasing solution pH. At freely corroding conditions, AA7075 exhibits preferential attack around the periphery pf Al_7Cu_2Fe, indicating matrix dissolution around the particles. Since Fe containing particles are cathodic to the matrix and have high cathodic kinetics, the presence of Fe in aluminum alloys is detrimental to the corrosion performance.

Zamin investigated the corrosion of a number of alloys with varying Fe and Mn concentration in ASTM G34 (EXCO test), which is an oxidizing acidic chloride environment[26]. The corrosion morphology was not noted, but the corrosion rate decreased with increasing Mn/Fe ratio because of a reduction in the potential difference between the IMPs and the matrix phase.

The electrochemical behavior evaluation of IMPs plays a significant role in understanding the localized corrosion of bulk aluminum alloys. However, in addition to the cathodic and anodic IMPs present in the alloy microstructure, the solid solution matrix phase also plays a critical role in alloy localized corrosion[27]. Potential-controlled experiments such as

Fig. 2 | SEM-EDS analysis of AA6xxx-T4 + PB, top surfaces (left), and cross-sections (right).
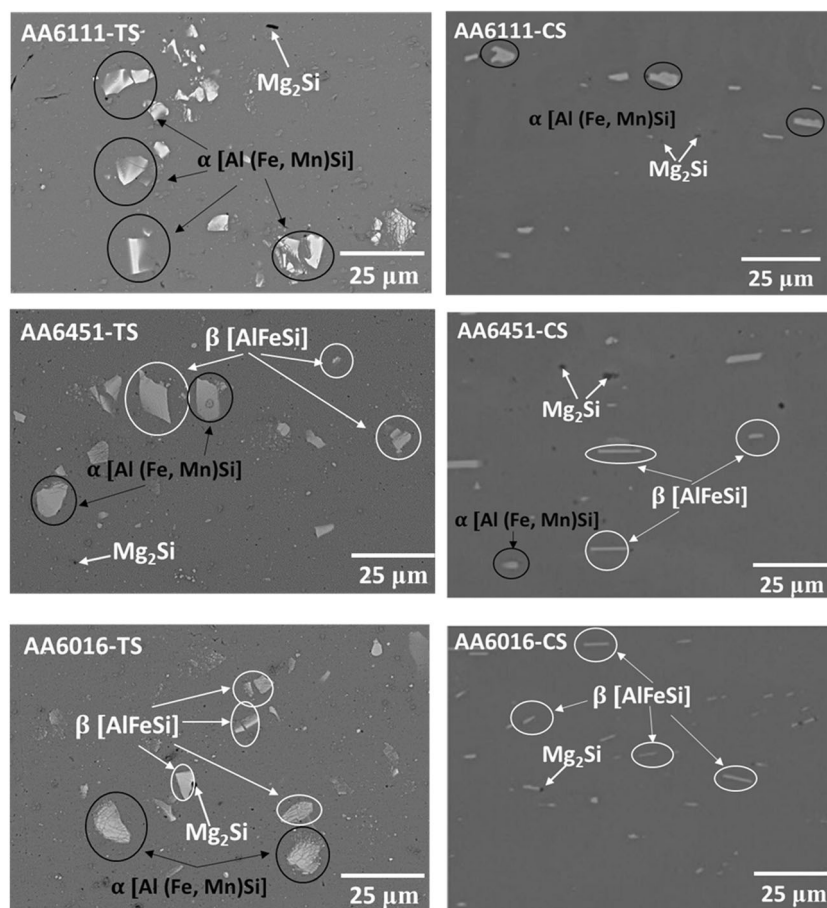
potentiodynamic polarization on bulk alloys might not be fully predictive because in such experiments the current required for the film breakdown is provided by the counter electrode, not the cathodic IMPs. At freely corroding conditions (i.e., at the open circuit potential) the simultaneous action of the matrix and IMPs is critical, so immersion experiments better reflect the corrosion performance during exposure in the field.

The goal of the present study is to understand the effects of microstructure and composition on the localized corrosion susceptibility of AA6111, AA6451 and AA6016 in aggressive chloride environments. In particular, the effects of α (Al_{15} (Fe,Mn)$_3$Si$_2$) and β (Al$_8$Fe$_2$Si), which are the primary large IMPs in AA6111 and AA6016, respectively, on the alloy corrosion susceptibilities are studied. The effects of the fine hardening phases are not considered. The microstructural and compositional analyses of the bulk alloys were performed using optical microscopy (OM), scanning electron microscopy- energy dispersive X-ray spectroscopy (SEM-EDS) and scanning transmission electron microscopy (STEM)-EDS. Quantitative analysis of the component phases was performed using X-ray diffraction (XRD). The electrochemical behavior of the bulk alloys was further evaluated using bulk analogs of the component phases, the alloy matrix phases, and the IMPs, which were fabricated by standard alloy casting procedures. The optimized bulk analogs were subjected to electrochemical testing using either macrocell or microcell approaches.

Results

Compositional and microstructural analyses of bulk alloys

The compositions of the three alloys are presented in Table 1. There are clear differences between the alloys in the alloying content of Si, Mg and Cu. In particular, AA6111 has higher Cu and Mg concentrations than AA6451 and AA6016. AA6016 has a higher Si content, resulting in high excess Si, which is the Si beyond what would be consumed in formation of α (Al_{15}

(Fe,Mn)$_3$Si$_2$), β (Al$_8$Fe$_2$Si) and Mg$_2$Si particles. Figure 1 shows optical micrographs of finely polished top surfaces of AA6xxx-T4 + PB, the alloys in the T4 plus paint bake condition. All the top surfaces exhibit dark IMPs of various sizes dispersed in a bright matrix. Some IMPs are darker than others, possibly due to compositional differences. Figure 2 shows SE micrographs of the polished top surfaces and cross-sections of the AA6xxx-T4 + PB. In these SE micrographs, the matrix is dark and dispersed with bright IMPs. EDS analysis on the top surfaces and cross-sections of AA6xxx has shown that the IMPs in AA6111 are mostly α and Mg$_2$Si, whereas those in AA6451 and AA6016 are α, β and Mg$_2$Si. The α IMPs are blocky in structure, the Mg$_2$Si particles are darker than the other IMPs, and β IMPs have a two-dimensional plate/needle-like structure.

Figures 3–5 show the STEM-EDS elemental maps of AA6111, AA6451, and AA6016, respectively. In the selected regions, AA6111 exhibited mostly α IMPs. AA6451 and AA6016 exhibited α, Mg$_2$Si, and elemental Si. β particles were not discerned in the elemental maps of AA6451 and AA6016.

Quantitative analysis of the IMPs in the alloys by XRD analysis is presented in Fig. 6. The results are given in vol.% of each IMP normalized by the total IMP content. Similar to the SEM-EDS results, XRD analysis also indicated that the IMPs in AA6111 were mostly α, ~93%, with the remaining ~ 7% being Mg$_2$Si phase. AA6451 contained ~59% α and ~37% β IMPs, with the remaining 4% being Mg$_2$Si phase. The IMPs in AA6016 were mostly β, ~60%, along with ~22% α and the remainder being elemental Si.

Evaluation of IGC susceptibility of bulk alloys

Figure 7 shows optical micrographs of top surfaces and cross-sections of AA6xxx-T4 + PB after testing by ISO 11846 B, which highlights IGC susceptibility. AA6111, with the higher Cu content, exhibited IGC attack and pitting corrosion on the top surface. In the cross-sectional view of AA6111,

Fig. 3 | STEM-EDS elemental analysis map of AA6111-T4 + PB top surface.
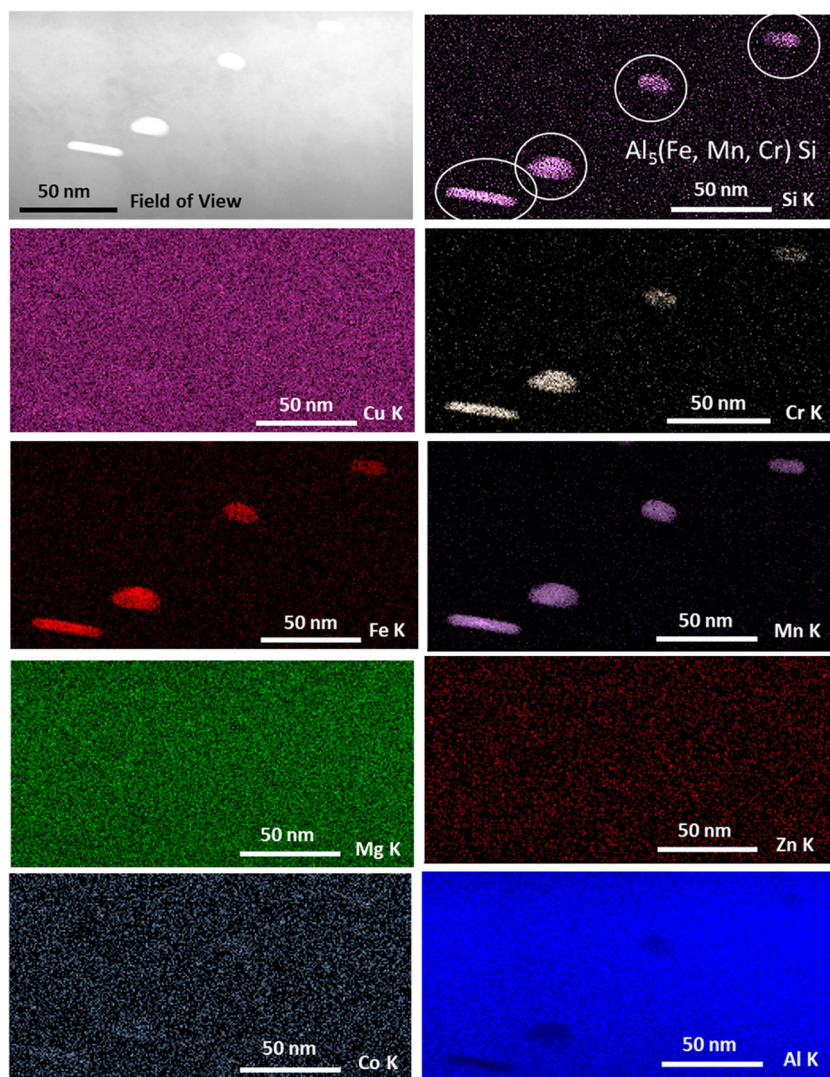
IGC attack can be seen to have penetrated ~10-15 μm beneath the surface. AA6451 and AA6016 exhibited severe pitting corrosion on the top surfaces but no IGC attack is evident. The cross-sections of AA6451 and AA6016 exhibited shallow IGC to 5 μm beneath the surface. The extent of IGC attack in AA6451 and AA6016 was clearly less than that observed in AA6111.

### Immersion testing in 5 wt.% NaCl

Figure 8 shows the optical micrographs of AA6xxx-T4 + PB subjected to immersion in 5 wt.% NaCl for 2 h, 48 h and 7 days. The 2 h immersion period provides information on the onset of corrosion, and all three alloys exhibited trenching around the large IMPs and pitting on the top surfaces after 2 h. The optical images indicate that AA6016 with low Cu content exhibited the greatest attack whereas AA6111 with higher Cu content exhibited the least attack. With increase in exposure time, the corrosion progressed, resulting in enlargement of the trenches in the matrix around the IMPs. The existing pits grew in size and new pits also formed. After 48 h of exposure, AA6016 exhibited the onset of grain boundary attack, AA6451 also exhibited traces of grain boundary etching, and AA6111 exhibited only trenching and pitting corrosion. After 7 days, grain boundary etching was very evident in AA6451 and AA6016. The specimens were removed from the solution after 7 days and optical micrographs of the cross-sections are shown in the bottom row of Fig. 8. Pitting is observed on the top surfaces of all three alloys and there is no evidence of IGC attack underneath the surface, which means the slight grain boundary attack was confined only to the very top surface. The cross-sections clearly indicate that AA6451 and AA6016 exhibited more severe attack than AA6111. The corrosion rates determined from the weight losses are presented in Table 2. AA6016 and AA6111 exhibited the highest and the lowest corrosion rates, respectively.

Potentiodynamic polarization of bulk alloys

Figure 9 shows the anodic polarization curves of the top surfaces of the three alloys. The values of E_{corr}, E_{pit} and i_{lim} determined from these curves all follow the decreasing trend: AA6111 > AA6451 > AA6016. Figure 10 shows the cumulative distribution plots of E_{pit} and E_{corr} of the alloys from 3-4 replicated experiments. AA6111 and AA6451 underwent pitting at E_{corr} as evidenced by the sharp increase in current as the potential was increased above E_{corr}. The low slope of the polarization curve suggests that the values of E_{corr} and E_{pit} are very close for these alloys and are therefore considered to be identical. In contrast, A6016 was spontaneously passive at E_{corr} and exhibited a passivity range of 25-50 mV before breakdown initiated. Standard interpretation of the potentiodynamic polarization curves by extrapolation of the anodic and cathodic portions of the curve to E_{corr} indicates that AA6016 and AA6111 should exhibit the lowest and the highest corrosion susceptibilities, respectively. However, as shown above, the reverse was observed in the neutral chloride exposure tests; AA6016 and AA6111 exhibited the highest and the lowest corrosion rates, respectively. In other words, the corrosion performances of the alloys during immersion testing were not predicted by the potentiodynamic polarization curves measured in the same environment.

Fig. 4 | STEM-EDS elemental analysis map of AA6451-T4 + PB, top surface.
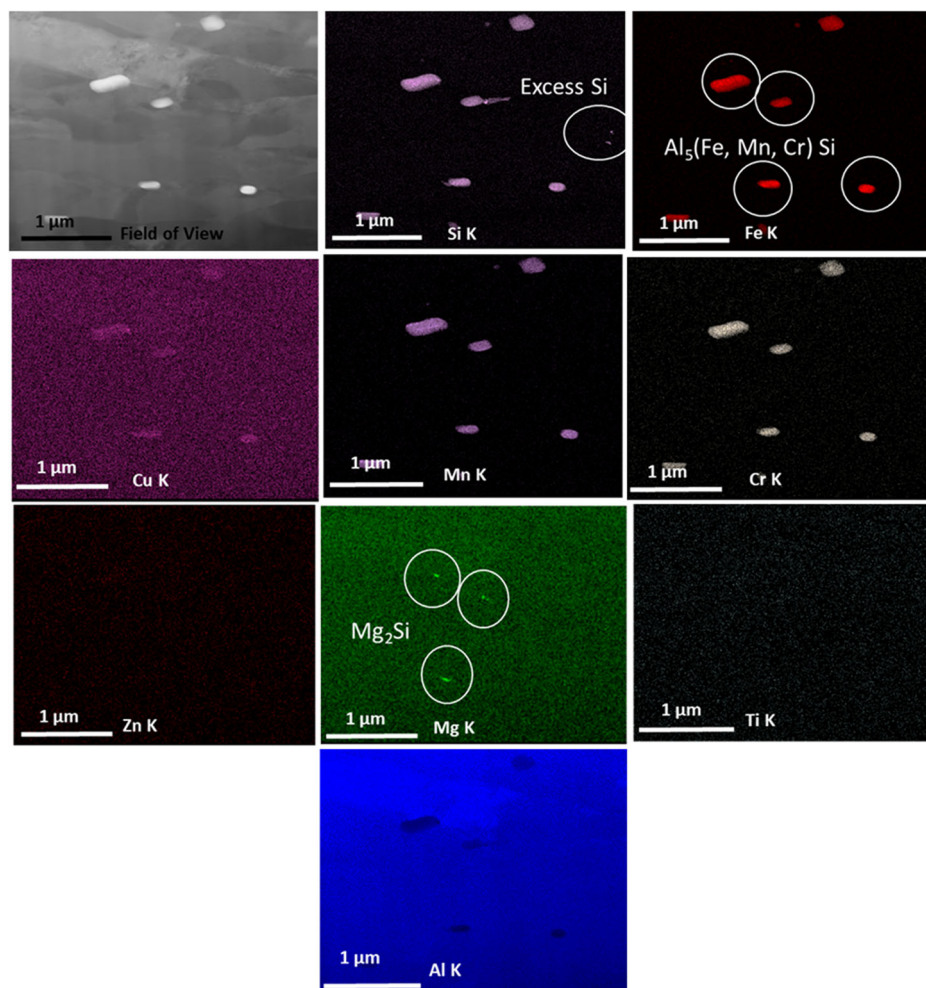
### Fabrication of bulk analogs of IMPs and matrix phase

To understand the corrosion behavior, experiments were performed on IMP and matrix individual analogs. The target composition of the AA6111 precipitate-free matrix analog was assessed by two different methods, SEM-EDS measurements at locations away from apparent IMPs and by Thermo-Calc™ calculations at 600 °C, and the results are presented in Table 3. Significant differences in the matrix composition from the two approaches are evident. The composition determined by SEM-EDS had higher content of every alloying element except Cu, probably because of inclusion of signal from small IMPs and subsurface IMPs that were not discerned in the SEM imaging. Both the SEM-EDS and Thermo-Calc™ compositions were cast, and microstructures were evaluated. Figure 11a, b show the optical micrographs of AA6111 matrix analogs cast using the SEM-EDS and Thermo-Calc™ compositions, respectively. The microstructure of the as-cast AA6111 matrix with composition from the SEM-EDS data exhibited unwanted phases along the grain boundaries whereas the Thermo-Calc™ matrix microstructure had smaller and fewer such phases. Therefore, the matrix composition determined using Thermo-Calc™ was considered to be more representative and was used for fabricating bulk analogs of the matrix of AA6451 and AA6016. These matrix analogs were also relatively free of precipitates. Table 4 shows the target compositions from Thermo-Calc™ calculations, and the compositions of the cast analogs measured by OES for the three alloys. The target compositions and the measured compositions of the cast analogs were quite similar. However, the Cu content measured in the cast analog of AA6111 matrix was half that of the target composition for an unknown reason. The as-cast matrix of AA6111 exhibited higher Cu content than AA6451 and AA6016 as intended.

The thermodynamic calculations performed for fabricating the α and β phases indicated that it is infeasible to cast 100% phase fraction of α and β as their cooling profiles predicted formation and co-existence of other undesirable phases. Also, the melting temperatures of pure α and β are very high, ~800–900 °C. Therefore, compositions that would result in formation of large areas of target IMP phases surrounded by an Al-rich phase were selected. The required weights of component master alloys were determined using Thermo-Calc™, melted in a furnace, and cast. Optical microscopy was performed on as-cast α and β IMPs, Fig. 12. The optical micrograph of as-cast α in Fig. 12a shows concentric rings of dark α with spacing of 15–20 μm and overall size of 50–150 μm. The microstructure of as-cast β, shown in Fig. 12b, exhibited a needle-like structure of dark β with a width of ~5–30 μm and spacing of 30–65 μm. Table 5 shows the comparison of compositions of target and as-cast α and β IMPs compositions. The as-cast α contained slightly higher Al concentration and lower concentrations of Fe and Mn than the target composition. The as-cast β contained slightly higher concentrations of Al and Fe than the target β composition. It can also be noted that the as-cast β had higher content of Fe than as-cast α.

Potentiodynamic polarization of bulk analogs of IMPs and matrix phase

The goal of the IMP fabrication was to create a structure with regions of IMP large enough to test using the microcell with a capillary diameter of 20–60 μm. To assess the ability of positioning the microcell on the IMP phases, potentiodynamic polarization experiments were performed on dark and bright phases in the optical micrographs of the as-cast α and β samples, where the dark phases are the target IMP structures. The polarization curves of the

Fig. 5 | STEM-EDS elemental analysis map of AA6016-T4 + PB, top surface.
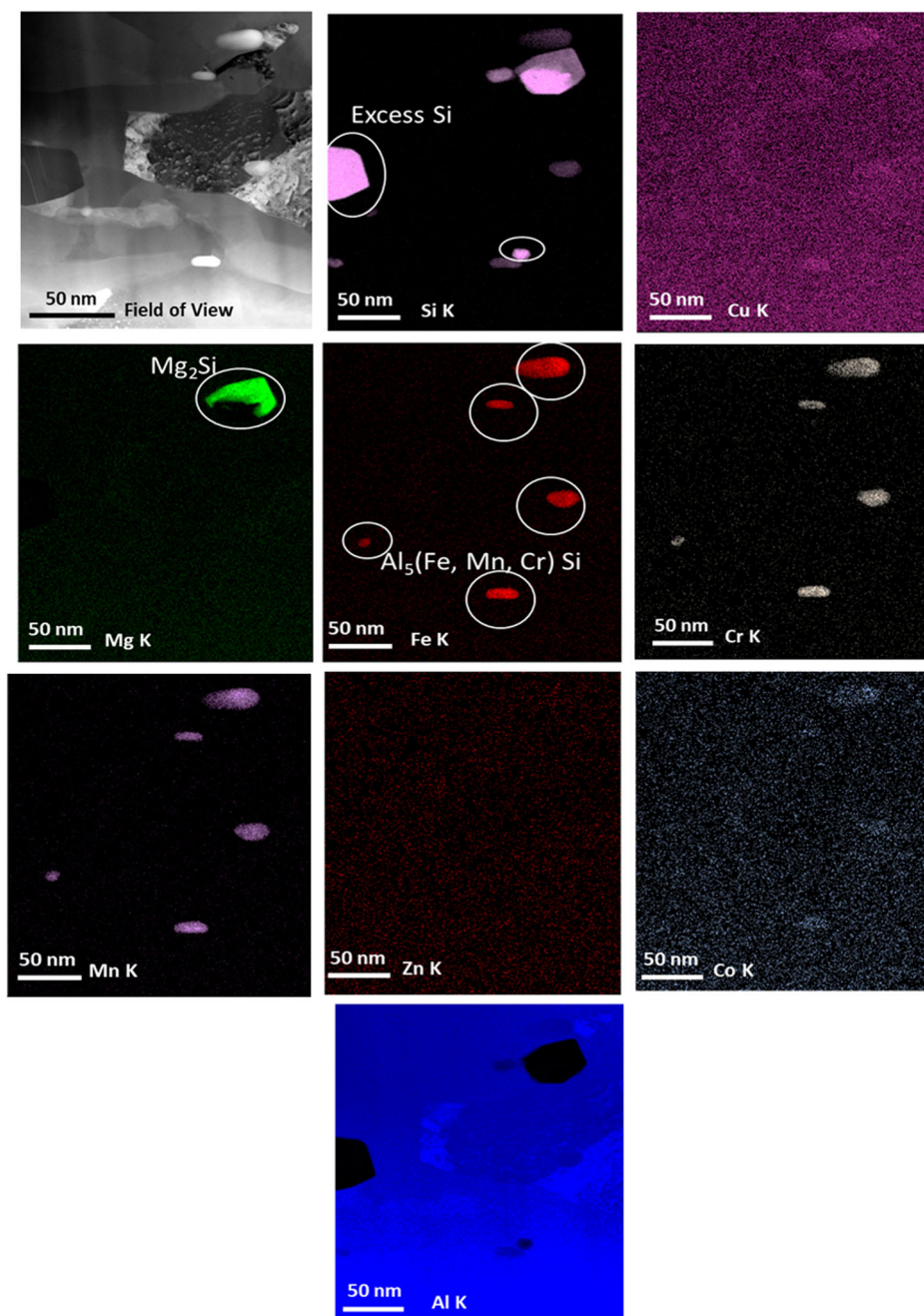
bright and the dark phases of as-cast α and β exhibited significant differences in the corrosion potentials and cathodic currents, Fig. 13. The bright phases, i.e., the continuous phases, had less noble E_{corr} (difference of ~200 mV) than their respective dark phases, i.e., the IMP phases. Comparison with these data provides an indication if the microcell was properly positioned within the dark phases in as-cast α and β analogs during the testing.

Figure 14 shows the cathodic polarization curves of as-cast α, as-cast β, and Si as well as anodic polarization curves from the as-cast matrix analogs for the three alloys, all measured using the microcell electrode setup. The E_{corr} values indicate that the as-cast IMPs and Si behave as cathodes and the AA matrix behaves as an anode when present together in a bulk alloy. The as-cast AA6111 matrix analog, which had higher Cu content, exhibited higher E_{pit} than AA6451 and AA6016 matrix analogs. However, its E_{corr} value was the lowest. The as-cast AA6111 matrix analog exhibits higher passive current density (i_{pass}) than AA6451 and AA6016 matrix analogs. β IMP exhibited more noble E_{corr} and higher cathodic kinetics than α IMP and

Si. The Si wafer was quite noble but exhibited low cathodic activity and so should be a less effective cathode when present, although the properties of Si will depend strongly on doping and defects.

Discussion
The optical micrographs of the three AA6xxx-T4 + PB (Fig. 1) are similar and show that some IMPs are darker than the others, possibly due to the difference in their compositions. SEM-EDS images of the top surfaces of the AA6xxx exhibited comparable particle number densities. Based on XRD analysis, the three AA6xxx exhibited different relative amounts of different IMPs: the IMPs in AA6111 were mostly α, AA6451 contained α, β and Mg$_2$Si in comparable proportions, and the majority of IMPs in AA6016 were β. The STEM-EDS elemental mapping was successful in detecting and identifying α, Mg$_2$Si and the elemental Si phases in AA6111, AA6451 and AA6016. However, β was not identified in AA6451 and AA6016 in STEM-EDS analysis.

AA6xxx-T4 + PB with higher Cu content exhibited traces of IGC during immersion testing in an acidic environment possibly due to microgalvanic corrosion between Cu enriched particles on the grain boundaries and a neighboring Cu-depleted zone. However, the overall extent of corrosion attack was higher in the low Cu-containing alloys as they experienced severe pitting. During immersion testing in a neutral chloride environment, which might be more representative of automotive exposure conditions than the acidic chloride environment, the high Cu-containing AA6111-T4 + PB also exhibited a lower corrosion rate than the other alloys. The low Cu content alloys exhibited severe pitting as well as slight IGC attack with increasing exposure time. In summary, considering the overall corrosion attack during immersion in both acidic and neutral environments, high Cu-containing AA6111-T4 + PB exhibited the best corrosion performance and low Cu-containing AA6016-T4 + PB exhibited the worst corrosion performance. These findings call into question the appropriateness of acidic chloride environments such as ISO 11846 B for assessing the suitability of materials for automotive applications. It is common to perform accelerated testing in environments more aggressive than expected service conditions. However, the test environment is inappropriate if the failure mode is changed. A concentrated chloride environment such as 5% NaCl solution might be more suitable for automotive materials selection.

In the potentiodynamic polarization curves, the top surface of AA6016-T4 + PB exhibited the lowest ORR limiting current density and the lowest i_{corr} followed by AA6451 and AA6111. The polarization curve for AA6016 was the only one that did not exhibit breakdown at the OCP. AA6111-T4 + PB, containing higher Cu content and a higher fraction of α IMPs than AA6451 and AA6016, exhibited more noble E_{corr} and E_{pit}. However, it exhibited pitting at E_{corr} and the highest i_{lim} for the ORR. Standard interpretation of polarization curves would conclude that the corrosion performance of AA6016 should be better than that of AA6111 in the T4 + PB condition.
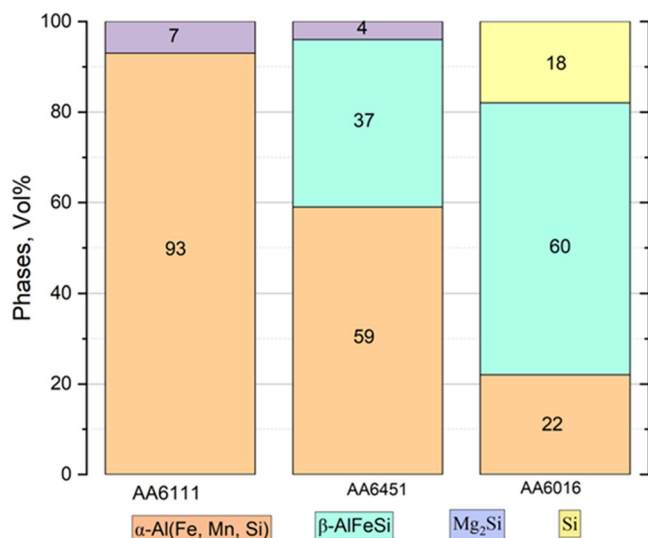

Fig. 6 | XRD-Quantitative analysis of AA6xxx-T4 + PB.

Fig. 7 | Optical micrographs of AA6xxx-T4 + PB tested under ISO 11846 B, top surfaces (left), and cross-sections (right).
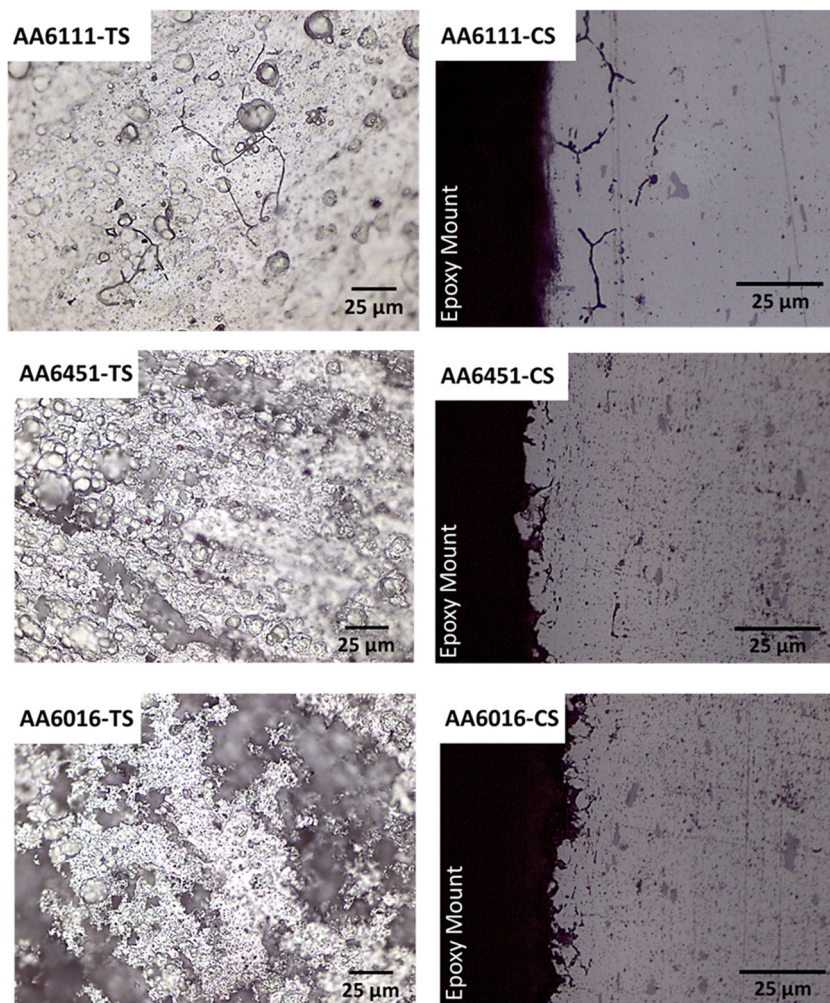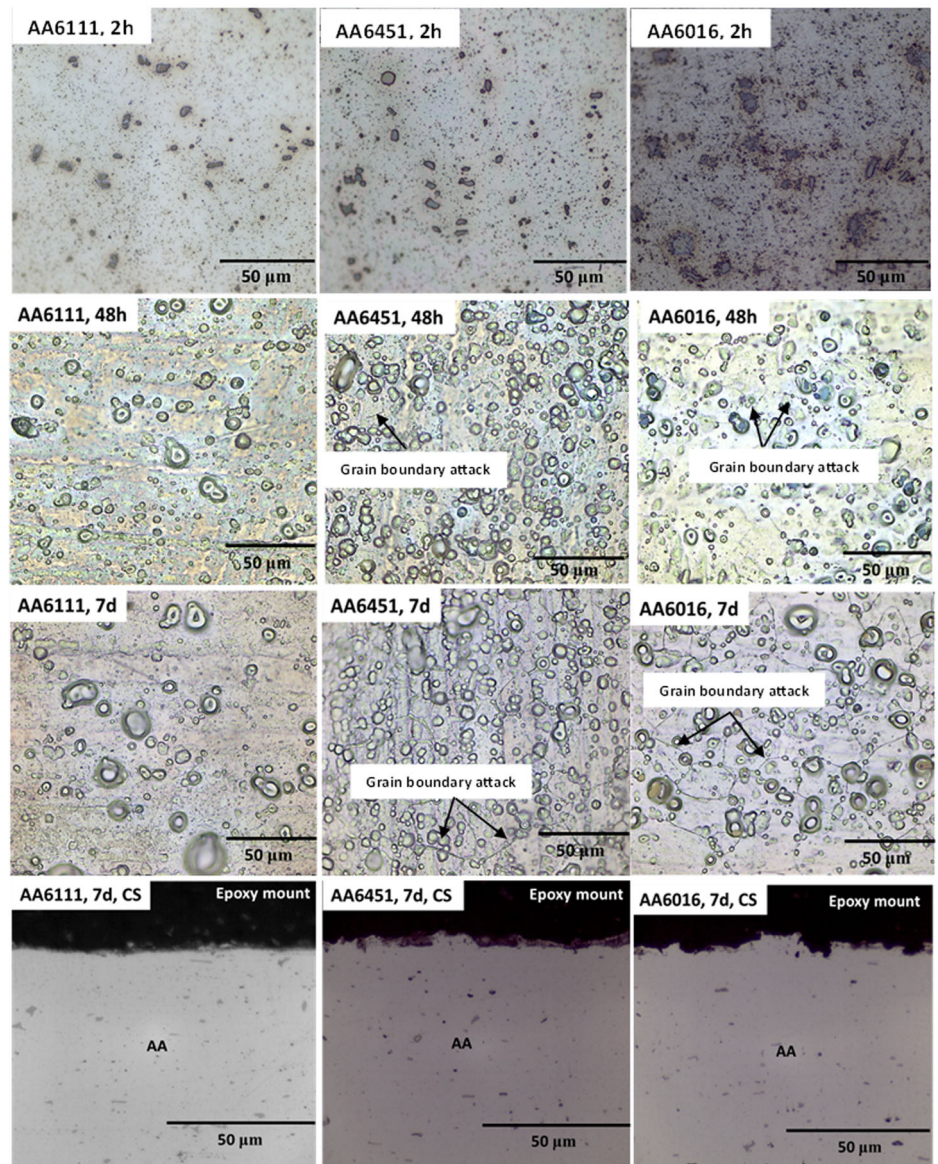
Fig. 8 | Optical micrographs of AA6xxx-T4 + PB, top surfaces and cross-sections, exposed to 5 wt.% NaCl to different exposure times.

The corrosion performances observed during the exposure tests followed the opposite trend of that predicted by the polarization curves. In the polarization experiments, which are potential-controlled experiments, the breakdown of the film at E_{pit} is driven by the potentiostat with current provided primarily via the counter electrode, not the cathodic IMPs. The nobility and catalytic characteristics of the IMPs should not be important in the anodic polarization curves if their only role is to act as cathodes; the matrix phase should play a more important role than the IMPs. In contrast, during immersion testing in acidic and neutral chloride environments at open circuit conditions, the corrosion characteristics of the AA6xxx are due to the interaction of the anodic matrix phase and cathodic IMPs phases

Table 2 | Corrosion rates determined after 5 wt.% NaCl exposure test

Alloy	Corrosion rate (mg/cm² day)
AA6111	0.046 ± 0.008
AA6451	0.055 ± 0.013
AA6016	0.071 ± 0.019

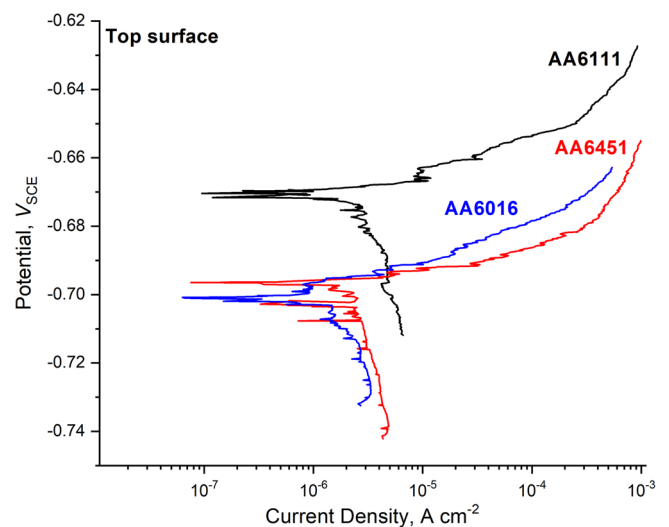The averages and deviations were determined from 3 replicate experiments

Fig. 9 | Potentiodynamic polarization curves of top surfaces of AA6xxx-T4 + PB tested using 3.5 wt.% NaCl, syringe cell setup.

during their microgalvanic coupling, including passive film breakdown, dissolution of matrix, ORR at IMPs, increase in pH at and near IMPs, and ohmic potential drops between local anodes and cathodes. Such interactions should also exist during real performance in the field. The differences in relative behavior of the alloys during immersion and potentiodynamic polarization tests might be the result of these differences in the influence of IMPs during the tests.

In this work, analogs of the alloy component phases were fabricated and tested separately by potentiodynamic polarization to achieve an understanding of their individual roles in the overall corrosion behavior of the bulk alloys. The potentiodynamic polarization curves of as-cast of AA6111, AA6451, and AA6016 matrix analogs, cast α and β IMP analogs and a Si wafer were determined. The intersections of the overlaid polarization curves provide an indication of how the phases might interact when they are exposed together in an alloy microstructure. Of course, the exact location of the intersection point and the details of the interaction will depend on factors such as area ratio and ohmic potential drops.
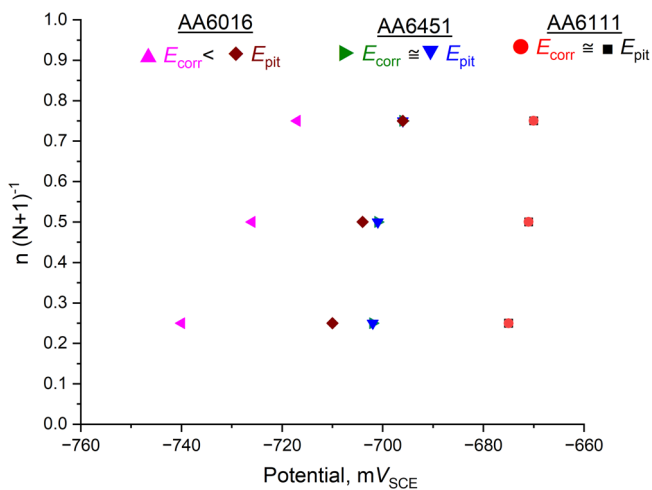

Fig. 10 | Cumulative distribution plot of E_{corr} and E_{pit} of AA6xxx subjected to polarization experiments in 3.5 wt.% NaCl. n is the ordinal number in the ordered list of values and N is the total number of specimens in the group.

Table 3 | AA6111-T4 + PB matrix composition determination using SEM/EDS and Thermo-Calc™ (version 2023 s) at 600 °C

Alloy matrix/ element wt. %	Si	Fe	Cu	Mn	Mg	Cr	Zn	Ti/Others	Al
SEM/EDS	0.99	0.17	0.43	0.13	2.02	0.08	0.06	0.08	96.01
Thermo-Calc prediction	0.41	0.02	0.49	0.11	0.75	0.05	0.03	0.03	98.10
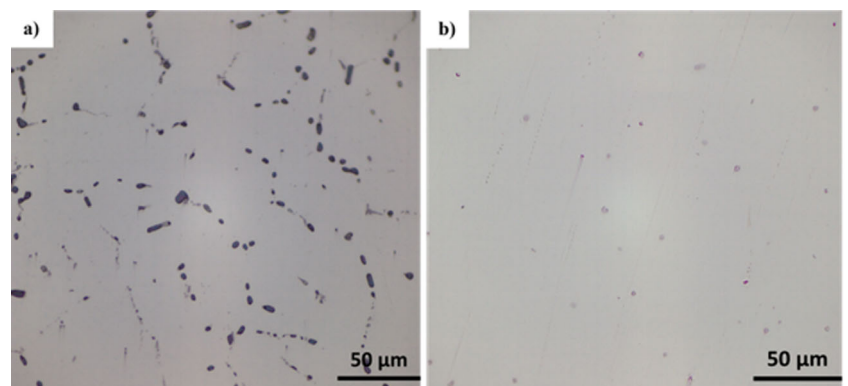
Nonetheless, an analysis of the polarization curve intersection points is instructive.

The AA6111 matrix phase analog with higher Cu content exhibits a higher E_{pit} and i_{pass} than AA6451 and AA6016 matrix phase analogs. β IMP exhibits a more noble E_{corr} and higher cathodic kinetics than α IMP. Table 4 shows that the Fe composition measured by OES was 10 and 22 at. % for the as cast α and β phases, respectively, which likely accounts for the difference in their cathodic kinetics. The cathodic curve of β intersects the anodic curves of AA6451 and AA6016 matrix analogs above their pitting potentials whereas the cathodic curve of α IMP intersects the anodic curve of AA6111 matrix analog in its passive region. If the i_{pass} for AA6111 were lower, then it is possible that the intersection with the cathodic curve of α IMP would be above the pitting potential. In this case, the high i_{pass} for AA6111 is beneficial. During open circuit exposure testing of AA6111-T4 + PB, the high Cu-containing matrix exhibiting high E_{pit} and i_{pass} combined with predominantly α IMPs with less Fe and reduced cathodic kinetics results in better overall corrosion performance than AA6016 with a lower Cu content matrix and predominantly β phase IMPs. Hence, for aluminum alloys where corrosion is controlled by combination of IMP activity and matrix susceptibility, potential-controlled experiments on the bulk alloys might not provide results that are reflective of exposure tests performed at open circuit conditions or field performance. This has important implications for the corrosion testing of many aluminum alloys.

Methods
Bulk alloy test materials and sample preparation for corrosion testing
AA6111, AA6451 and AA6016 in the T4 temper (comprising solution heat treatment at 1050 ˚F, water quenching and natural aging), were provided by Novelis Inc. The thicknesses of AA6111, AA6451 and AA6016 sheets were 2, 0.9 and 0.9 mm, respectively. The elemental compositions of the as received 6xxx alloys were obtained from the internet (matweb) and confirmed using arc spark optical emission spectrometry (spark-OES) and are presented in Table 1. Prior to all the experiments, samples were cleaned using ethanol to remove dirt and other contamination. The Al alloy sheets were subjected to a simulated paint bake (PB) treatment by heating at 180 °C in a laboratory oven furnace for 20 min.

Compositional and microstructural examination of bulk alloys
Al alloy samples were prepared for microscopic examination and electrochemical experiments by grinding to #1200 using SiC papers, followed by polishing using 3 μm and 1 μm diamond pastes and finally with 0.05 μm colloidal silica. Optical microscopy was performed on AA6xxx-T4 + PB samples using an Olympus GX53™ inverted optical microscope. Microstructural and compositional analyses of AA6xxx-T4 + PB samples were also performed using a Thermo Scientific Apreo™ SEM- EDS and Themis-Z™ STEM-EDS at CEMAS, OSU. X-ray diffraction analysis was performed at Novelis Inc.

Fig. 11 | Optical micrographs of as-cast AA6111 matrix samples. a Composition from SEM-EDS. **b** Composition from Thermo-Calc™.

IGC testing of bulk alloys using ISO 11846

To determine the IGC susceptibilities, alloy samples were subjected to ISO 11846 Method B testing[28]. The method involves the following steps of sample preparation: degreasing with ethanol, deoxidizing by alkaline etching in 5% NaOH at 80 °C for 60 s and desmutting in concentrated HNO_3 for 30 s. The samples were rinsed with DI water between the steps and after desmutting. Finally, the Al alloy samples of size 2 cm×1.5 cm were immersed in an aqueous solution consisting of 30 g NaCl and 10 ml concentrated HCl per 1000 ml solution, for 24 h. The pH of the solution was measured to be 0.8 - 1. After the exposure, the samples were rinsed with DI water and desmutted by immersion in concentrated HNO_3 for 30 min. Optical microscopy was performed on the top surfaces and mounted cross-sections of the three alloys to determine the extent of IGC attack.

Immersion testing of bulk alloys in 5 wt.% NaCl

Alloy samples were immersed in 5 wt.% NaCl solution (pH 6.5) for 7 days. The extent of corrosion was determined by collecting optical micrographs after 2 h, 48 h and 7 days of exposure. After the exposure, the corrosion product was removed by immersion in concentrated HNO_3 for 30 min and rinsing with DI water. The average corrosion rates were determined from the weight loss, and the exposed surfaces were examined by optical microscopy.

Potentiodynamic polarization testing of bulk alloys

Potentiodynamic polarization experiments on the Al alloy samples were performed using either a syringe cell setup[29] or a microcell capillary (electrode) setup[7,27] based on the size of the test area. The top surfaces were tested using the syringe cell setup and the fabricated bulk analogs samples were tested using the microcell capillary setup. In both setups, a platinum wire, and a saturated calomel electrode (SCE) were used as the counter and reference electrodes, respectively. The test electrolyte was 3.5 wt.% NaCl open to air. All the samples were exposed at their open circuit potentials (OCP) for 300 s prior to anodic and cathodic potential scans were performed separately. The anodic polarization scans in the syringe cell involved polarization of the samples from 30 mV below the OCP to -600 mV_{SCE} at a scan rate of 0.167 mV s^{-1}. The scan rate was 2 mV s^{-1} in the microcell electrode setup to minimize test duration. During cathodic polarization scans, samples were polarized from 20 mV above the OCP to -900 mV_{SCE}. The exposed test area in the syringe cell setup was approximated to be the inner diameter of the syringe cell opening, ~3.8 mm for a 60 mL syringe, which resulted in a test area of 0.11 cm^2. Although the exposure area was smaller than that typically used for corrosion measurements, it is large relative to the microstructure, so the technique is considered to be a macroscale measurement. The typical diameter of the microcell electrode was 20-60 μm and the test area for each trial was determined by examining the exposed area after the polarization scan under an optical microscope. Three or four replicate measurements were performed on each sample type. The corrosion potential (E_{corr}), pitting potential (E_{pit}), limiting current density (i_{lim}), galvanic potential (E_{galv}), and galvanic current density (i_{galv}) were determined from representative polarization curves.

Fabrication and corrosion testing of bulk analogs of IMPs and matrix phase

Bulk analogs of the principal intermetallic phases in AA6111, AA6451, and AA6016, which are α (Al_{15} (Fe,Mn)$_3Si_2$) and β (Al_8Fe_2Si), and the matrix phases were cast using compositions predicted by the Thermo-Calc™ thermodynamic calculations software (version 2023a) and measurements by SEM-EDS. The Thermo-Calc™ calculations were performed at 600 °C, which was indicated by the software as the solidus temperature. The SEM-EDS analysis was performed on an area ~0.125 μm^2 at a location that was free of apparent IMPs. The elemental components were heated to 750 °C, which melted all the solid materials. Overheating the components was avoided to restrict atmospheric hydrogen from dissolving into the melt. The liquid alloy was poured into a silica crucible followed by air cooling. The motivation for fabrication of matrix bulk analogs was to be able to perform electrochemical testing on regions of alloy matrix in which there were no other phases. The

Table 4 | Matrix compositions of target and As-cast materials using Thermo-Calc™ at 600 °C and OES

Element/ At.%	AA6111		AA6451		AA6016	
	T-Calc	Measured	T-Calc	Measured	T-Calc	Measured
Si	0.41	0.32	0.62	0.64	0.78	0.76
Cu	0.21	0.1	0.04	0.001	0.03	0.00
Fe	0.01	0.02	0.01	0.05	0.01	0.05
Mn	0.05	0.01	0.01	0.001	0.002	0.001
Mg	0.84	0.72	0.68	0.70	0.24	0.27
Ti	0.02	0.01	0.01	0.01	0.02	0.01
Zn	0.01	0.02	-	-	0.04	0.02
Cr	0.03	0.01	0.01	-	0.001	-
Al	98.42	99.14	98.63	98.58	98.84	98.86

Table 5 | EDS-compositional analysis of target and As-cast IMP phases

IMP phase	Sample condition	Composition, at. fraction	Fe composition, at%
α	Target	Al_{15} (Fe, Mn)$_3$ Si$_2$	0–19
	As cast	$Al_{16.5}$ Fe$_2$ Mn$_{1.2}$ Si$_2$	10
β	Target	Al_8 Fe$_2$ Si	17
	As cast	$Al_{10.5}$ Fe$_{3.2}$ Si	22

Fig. 12 | Optical micrographs of as-cast IMP samples. a α – (Al, Fe, Mn, Si) IMP, **b** β – (Al, Fe, Si) IMP.
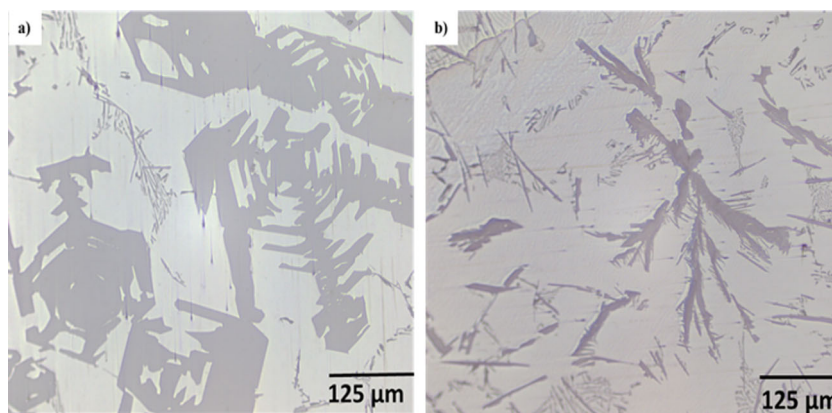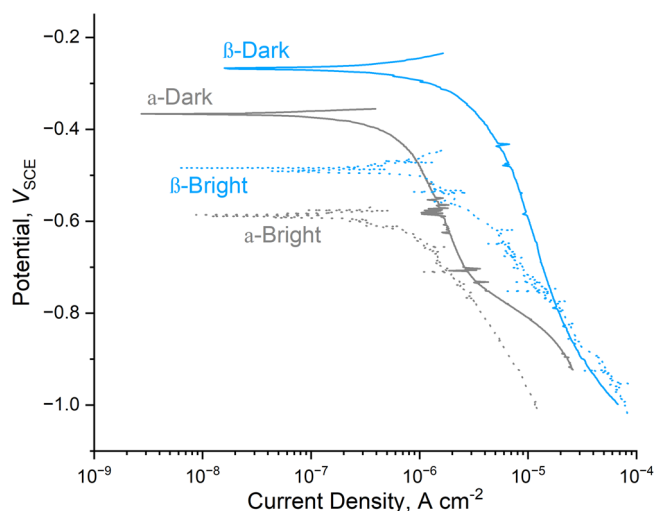
Fig. 13 | Potentiodynamic polarization curves of as-cast α and β IMPs; tests performed on dark and bright regions.
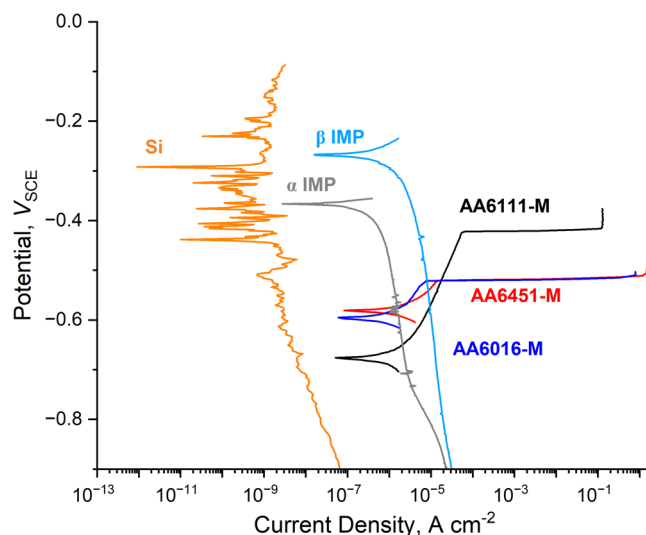

Fig. 14 | Potentiodynamic polarization curves of as-cast matrices, α, β, and Si phases.

optimum composition of the fabricated matrix phase analogs was selected based on the microstructures of the cast materials. The α and β IMP compositions were selected based on predictions from Thermo-Calc™. Optical microscopy was performed on the cast α and β structures, and SEM-EDS analysis was performed to determine the compositions of the cast materials. To simulate the electrochemical behavior of elemental Si, testing was performed on a n-type Si wafer with a dopant concentration of ~10^{18} cm^{-3}.

Data availability

Data supporting the findings of this study are available from the corresponding author upon request.

References

1. Davis, J. R. Alloying: understanding the basis. *In:* Alloying: understanding the basics, 351–416 (ASM International, 2001).
2. Frankel, G. S. Pitting corrosion of metals: a review of the critical factors. *J. Electrochem. Soc.* **145**, 2186–2198 (1998).
3. Szklarska-Smialowska, Z. Pitting corrosion of aluminum. *Corros. Sci.* **41**, 1743–1767 (1999).
4. Davis, J. R. Corrosion of aluminum and aluminum alloys. *In:* Corrosion of aluminum and aluminum alloys 1–24 (1999).
5. Shercliff, H. R. & Ashby, M. F. A process model for age hardening of Aluminium alloys-I. The model. *Actta Met. mater.* **38**, 1789–1802 (1990).
6. Buchheit, R. G. A compilation of corrosion potentials reported for intermetallic phases in aluminum alloys. *J. Electrochem. Soc.* **142**, 3994–3996 (1995).
7. Birbilis, N. & Buchheit, R. G. Electrochemical characteristics of intermetallic phases in aluminum alloys. *J. Electrochem. Soc.* **152**, B140 (2005).
8. Mukhopadhyay, P. Alloy designation, processing, and use of AA6XXX series aluminium alloys. *ISRN Met.* **2012**, 1–15 (2012).
9. Ng, C.-H., Yahaya, S. N. & Majid, A. A. Reviews on aluminum alloy series and its applications. *Acad. J. Sci. Res* **5**, 708–716 (2017).
10. Hatch, J. E. Aluminum: properties and physical metallurgy. (ASM, 1984).
11. Cole, G. S. & Sherman, A. M. Light weight materials for automotive applications. *Mater. Charact.* **35**, 3–9 (1995).
12. Adapala, P., Hosking, N., Nichols, M. & Frankel, G. S. Laboratory accelerated cyclic corrosion testing and on-road corrosion testing of AA6××× coupled to carbon fiber-reinforced plastics. *Corrosion* **78**, 599–611 (2022).
13. Mullert, L. & Galvele, J. R. Pitting potential of high purity binary aluminum alloys-I. Al-Cu alloys pitting and intergranular corrosion. *Corros. Sci.* **17**, 179–193 (1977).
14. Larsen, M. H., Walmsley, J. C., Lunder, O. & Nisancioglu, K. Effect of excess silicon and small copper content on intergranular corrosion of 6000-series aluminum alloys. *J. Electrochem. Soc.* **157**, C61 (2009).
15. Larsen, M. H., Walmsley, J. C., Lunder, O., Mathiesen, R. H. & Nisancioglu, K. Intergranular corrosion of copper-containing AA6xxx AlMgSi aluminum alloys. *J. Electrochem. Soc.* **155**, C550 (2008).
16. Zou, Y. et al. The intergranular corrosion behavior of 6000-series alloys with different Mg/Si and Cu content. *Appl. Surf. Sci.* **405**, 489–496 (2017).
17. Svenningsen, G. et al. Effect of low copper content and heat treatment on intergranular corrosion of model AlMgSi alloys. *Corros. Sci.* **48**, 226–242 (2006).
18. Svenningsen, G., Larsen, M. H., Walmsley, J. C., Nordlien, J. H. & Nisancioglu, K. Effect of artificial aging on intergranular corrosion of extruded AlMgSi alloy with small Cu content. *Corros. Sci.* **48**, 1528–1543 (2006).
19. Kairy, S. K., Rometsch, P. A., Davies, C. H. J. & Birbilis, N. On the intergranular corrosion and hardness evolution of 6xxx series Al alloys as a function of Si:Mg ratio, Cu content, and aging condition. *Corrosion* **73**, 1280–1295 (2017).
20. Kairy, S. K. et al. Exploring the electrochemistry of 6xxx series aluminium alloys as a function of Si to Mg ratio, Cu content, ageing conditions and microstructure. *Electrochim. Acta* **190**, 92–103 (2016).
21. Dorin, T., Stanford, N., Birbilis, N. & Gupta, R. K. Influence of cooling rate on the microstructure and corrosion behavior of Al-Fe alloys. *Corros. Sci.* **100**, 396–403 (2015).
22. Seri, O. The effect of NaCl concentration on the corrosion behavior of aluminum containing Iron. *Corros. Sci.* **36**, 1789–1803 (1994).
23. Osório, W. R., Peixoto, L. C., Goulart, P. R. & Garcia, A. Electrochemical corrosion parameters of as-cast Al-Fe alloys in a NaCl solution. *Corros. Sci.* **52**, 2979–2993 (2010).
24. Birbilis, N., Cavanaugh, M. K. & Buchheit, R. G. Electrochemical behavior and localized corrosion associated with Al7Cu2Fe particles in aluminum alloy 7075-T651. *Corros. Sci.* **48**, 4202–4215 (2006).
25. Park, J. O., Paik, C. H., Huang, Y. H. & Alkire, R. C. Influence of Fe-rich intermetallic inclusions on pit initiation on aluminum alloys in aerated NaCl. *J. Electrochem. Soc.* **146**, 517–523 (1999).

26. Zamin, M. Role of mn in the corrosion behavior of al-mn alloys. *Corrosion* **37**, 627–632 (1981).
27. Buchheit, R. G. et al. The electrochemistry of intermetallic particles and localized corrosion in Al alloys. *JOM* **53**, 29–33 (2001).
28. Schnatterer, C., Bulinger, A. & Zander, D. Evaluating the intergranular corrosion susceptibility of Al-Mg-Si-Cu alloys using electrochemical methods. *Mater. Corros.* **67**, 1308–1313 (2016).
29. Panindre, A. M., Chang, K. H., Weirich, T. & Frankel, G. S. Technical note: syringe cell for electrochemical testing. *Corrosion* **74**, 847–850 (2018).

Author contributions
P.A.: conceptualization, investigation, writing—original draft, writing—review & editing. T.A.: conceptualization, investigation. Y.Y: conceptualization. M.L.L., G.B., S.D., A.L.: conceptualization, writing—review & editing. G.S.F: conceptualization, writing—original draft, writing—review & editing.

Competing interests
The authors declare no competing interests.

Additional information
Correspondence and requests for materials should be addressed to Gerald S. Frankel.

Reprints and permissions information is available at http://www.nature.com/reprints

Publisher's note Springer Nature remains neutral with regard to jurisdictional claims in published maps and institutional affiliations.